

Research Article

Neural Network and Performance Analysis for a Novel Reconfigurable Parallel Manipulator Based on the Spatial Multiloop Overconstrained Mechanism

Guanyu Huang ^{1,2}, Dan Zhang ² and Qi Zou²

¹Zhejiang Lab, 1818 Wenyi West Road, Hangzhou 311121, China

²Department of Mechanical Engineering, Lassonde School of Engineering, York University, 4700 Keele Street, Toronto, ON, Canada M3J 1P3

Correspondence should be addressed to Dan Zhang; dzhang99@yorku.ca

Received 16 April 2020; Revised 23 June 2020; Accepted 30 June 2020; Published 25 August 2020

Academic Editor: Mohammad Tawfik

Copyright © 2020 Guanyu Huang et al. This is an open access article distributed under the Creative Commons Attribution License, which permits unrestricted use, distribution, and reproduction in any medium, provided the original work is properly cited.

To meet the different requirements in the industrial area, a novel reconfigurable parallel mechanism is proposed based on the spatial multiloop overconstrained mechanism. The configurations can be changed by driving the low-DOF (degree-of-freedom) overconstrained mechanism. The mobility of this mechanism is investigated. And the kinematic model and Jacobian matrix are both established. Based on the Jacobian matrix, the workspace, stiffness, and conditional number are all analyzed. To focus on the application in the industrial area, this paper proposes a method to establish the relationship between the performance and the structural parameters by using the modified BP neural network. Based on this method, the structural parameters can be chosen by the requirements of the special task in the industrial area. Finally, some numerical examples are presented to verify the method.

1. Introduction

Recently, parallel mechanisms have gained more and more interests in the research community, due to their advantages caused by their structures, like high stiffness, good dynamic performance, and high load [1–4]. However, in the modern industrial area, the parallel mechanisms with a single performance cannot meet the requirements of the flexible manufacturing systems. In this case, the reconfigurable parallel mechanisms have been the hot area in the parallel mechanism field. In order to obtain a novel reconfigurable parallel mechanism, researchers presented many ways, like modularity [5–7], metamorphic link or joint [8–10], and reconfigurable link [11, 12] or mechanism [2]. The initial reconfigurable parallel mechanisms are proposed using the modularization, which can change their configuration by adding or locking some modular components. To change the based platform, the Bicept robot has different configurations, which was presented by Li et al. [5]. These reconfigurable parallel mechanisms cannot change their configurations

by themselves, and the reconfiguration processes need manual intervention. Thus, some metamorphic structures have been proposed to make mechanisms change their configuration. By using the Bennett plano-spherical mechanism, Zhang et al. [8] presented a novel reconfigurable parallel mechanism. The mechanism has a different configuration by altering some metamorphic joints or linkages into different working phases. Similar to this way, another metamorphic parallel mechanism has been proposed [13]. At the same time, some lockable joints have been proposed to change the mechanisms' configuration [9, 14–16]. In this way, the mechanisms should go through the singularity position when the mechanisms change their configurations. So, they cannot change their configurations, continuously. Thus, a new way to design the reconfigurable parallel mechanism attracted more and more researchers, which is using the reconfigurable link or mechanism.

Performance evaluation for the parallel mechanism is a significant issue in real industrial application [17]; thus, some indices have been proposed to evaluate the workspace [18–20],

stiffness [21], and other aspects [22–24] of the mechanism. In this case, the performance analysis of reconfigurable parallel mechanisms has also gained interests. Coppola et al. [25] presented a reconfigurable hybrid robot called ReSI-Bot, and some performance like workspace, singularity, and stiffness were all discussed. Huang et al. [26] proposed a 5-DOF reconfigurable hybrid robot named TriVariant, and minimizing a global and comprehensive conditioning index was used to optimize its structural parameter. Based on the virtual coefficient, Wang et al. [27] proposed a generalized transmission index that can evaluate the motion/force transmissibility of fully parallel manipulators, while, in this paper, the overconstrained mechanism is applied to build a novel reconfigurable parallel mechanism with different configurations [28]. Compared with the existing method, the proposed mechanism can continuously change its configuration without human intervention. For the workspace of a reconfigurable parallel mechanism, Brisan and Csiszar [29] proposed some novel workspace indices to investigate the relationship between the shape, dimensions of the workspace, and the configurations of the mechanism. Viegas et al. [30] proposed three strategies including drive range extension, base translation, and dynamic joint reconfiguration to research the workspace of the reconfigurable spatial parallel mechanism. Chen [31] proposed a novel performance index to evaluate the maximum dynamic load-carrying capacity (DLCC) by using Boltzmann-Hamel-d'Alembert formalism.

However, the above performance indices are obtained after the mechanisms are determined. Well, for the reconfigurable parallel mechanisms, the most significant characteristic is that they have many different performances. In order to choose a certain configuration based on the requirement, combining artificial intelligence and parallel mechanism is a considerable method to establish the relationship between the performance and configuration.

With the intersection of mechanism and artificial intelligence, the intelligent algorithms are widely used to optimize the mechanism structural parameters [32–34], solve the kinematic solution [35, 36], plan the trajectory of the end effector [37, 38], and so on. Based on the genetic algorithm, Kelaiaia et al. [39] focused on the multiobjective optimization of a linear Delta parallel robot, regarding workspace, stiffness, kinematic, and dynamic performances as the criteria. Jamwal et al. [40] proposed a novel ankle rehabilitation robot, based on the modified genetic algorithm; the kinematic design optimization for the parallel robot was proposed. Based on the neural network, the analytical solutions of system stiffness and dexterity for a spatial parallel mechanism were calculated [41]. According to different machining requirements, single-objective optimization and multiobjective optimization algorithms were both used to optimize a serial-parallel hybrid polishing machine tool [42]. Zhang and Lei [35] used the artificial neural network to solve the forward kinematic problem of the parallel mechanism. To optimize the serial-parallel hybrid polishing machine tool, Wang et al. proposed a method to balance the machining quality and efficiency by using a neural network.

To solve the above problem that task oriented configuration determination, this paper proposes a novel method to establish the relationship between the performance indices and structural parameters by using the modified BP neural network. Based on this neural network, import the performance requirements and the structural parameters can be exported. In this way, the configuration can be determined by the special task.

In this paper, a novel reconfigurable parallel mechanism is presented, based on the spatial multiloop overconstrained mechanism. Next, the kinematic and dynamic models are both established. Then, the performance analysis for the proposed mechanism is processed. Next, according to the industrial requirements, a novel BP neural network is established to obtain the relationship between the configurations and performance indices. Finally, some numerical examples are presented to verify the correctness of these analyses.

2. Design Description

2.1. Model Description. The schematic of the proposed reconfigurable parallel mechanism is shown in Figure 1. The reconfigurable mechanism consists of a spatial overconstrained mechanism and a parallel mechanism. The spatial overconstrained mechanism has three identical limbs, and each limb has one horizontal joint and one revolution joint. At the same time, the parallel mechanism also has three identical limbs and each limb has three joints which are the vertical prismatic joint and two universal joints. Each limb is connected to the based platform by a horizontal joint, so the limb can move along the axis of the horizontal joint, while a connecting link connected the limbs 1 and 2, and the two sides of the link are both revolute joints, so is the relationship between limbs 2 and 3. In this case, the based platform, three vertical links, and two connecting links comprise the spatial multiloop overconstrained mechanism, which has one degree of freedom (DOF). And its DOF will be proved in the following section.

The parallel mechanism consists of three identical limbs arranged by a vertical prismatic joint and two universal joints. When the spatial multiloop overconstrained mechanism is drove, the structural parameter of the parallel mechanism will be changed; then, the whole manipulator owns different configurations, which means the reconfigurable parallel mechanism has different performance. For this manipulator, the horizontal prismatic joints and the vertical prismatic joints are regarded as the actuators.

2.2. Mobility Analysis. In this section, the mobility of the manipulator is analyzed, especially for the spatial multiloop overconstrained mechanism. The initial position of the manipulator is shown in Figure 1. The fixed coordinate system is located at the central point of the based platform, which is expressed by $O-xyz$. The coordinates of each point belonged to the spatial multiloop mechanism can be written as $A_1 = [x_{a1} \ y_{b1} \ z_{a1}]^T$, $E_1 = [x_{e1} \ y_{e1} \ z_{e1}]^T$, $A_2 = [x_{a2} \ y_{b2} \ z_{a2}]^T$, $E_2 = [x_{e2} \ y_{e2} \ z_{e2}]^T$, $A_3 = [x_{a3} \ y_{b3} \ z_{a3}]^T$, and $E_3 = [x_{e3} \ y_{e3} \ z_{e3}]^T$, separately.

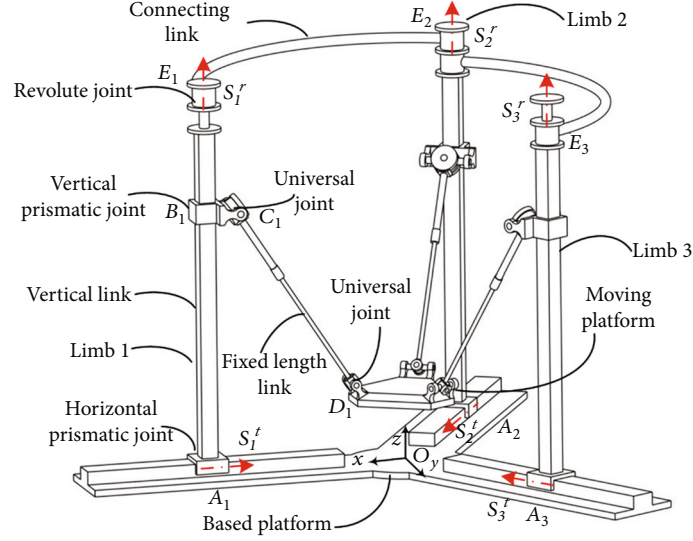


FIGURE 1: The schematic of the reconfigurable parallel mechanism.

Based on the *screw theory*, in the limb A_1E_1 , the direction of the horizontal prismatic joint, A_1 , is along the x -axis, which can be written as $[1 \ 0 \ 0]^T$. The axial direction of the revolute joint, E_1 , is $[0 \ 0 \ 1]^T$; thus, the twist screw can be written as

$$\begin{cases} \$1^t = [0 \ 0 \ 0; \ 1 \ 0 \ 0]^T, \\ \$1^r = [0 \ 0 \ 1; \ 0 \ x_{e1} \ 0]^T. \end{cases} \quad (1)$$

Based on Equation (1), the wrench system of the limb A_1E_1 can be written as

$$\begin{cases} \$1^r = \begin{bmatrix} 0 & 0 & 0; & 0 & 0 & 1 \\ 0 & 0 & 0; & 0 & 1 & 0 \\ 0 & 1 & 0; & 0 & 0 & -x_{e1} \\ 0 & 0 & 1; & 0 & 0 & 0 \end{bmatrix}^T, \end{cases} \quad (2)$$

Similarly, for the limb A_2E_2 , the axial direction of the horizontal prismatic joint, A_2 , is $[a_1 \ b_1 \ 0]^T$ and the axial direction of the revolute joint, E_2 , is along with the z -axis, which can be written as $[0 \ 0 \ 1]^T$; thus, the twist system of the limb A_2B_2 is

$$\begin{cases} \$1^t = [0 \ 0 \ 0; \ a \ b \ 0]^T, \\ \$1^r = [0 \ 0 \ 1; \ 0 \ x_{e2} \ 0]^T. \end{cases} \quad (3)$$

Based on Equation (3), the wrench system of the limb A_2B_2 can be written as

$$\begin{cases} \$2^t = \begin{bmatrix} 0 & 0 & 0; & 0 & 0 & 1 \\ 0 & 0 & 0; & 0 & 1 & 0 \\ -\frac{b_1}{a_1} & 1 & 0; & 0 & 0 & x_{e2} \\ 0 & 0 & 1; & 0 & 0 & 0 \end{bmatrix}^T, \end{cases} \quad (4)$$

Based on Equations (2) and (4), the twist system of the spatial single-loop overconstrained mechanism can be obtained as

$$\$_{A1A2} = \begin{bmatrix} 0 & 0 & \frac{1}{x_{e1}}; & \frac{a(x_{e1} + x_{e2})}{bx_{e1}} & 1 & 0 \end{bmatrix}^T. \quad (5)$$

According to Equation (5), the single-loop overconstrained mechanism has one DOF, and the mobility of the other single-loop mechanism including limbs A_2B_2 and A_3B_3 can be calculated in the same way.

The proposed spatial multiloop overconstrained mechanism consists of the two single-loop mechanisms, and the limb A_2B_2 is the common limb, which is attached to the driving joint. In this case, the spatial multiloop overconstrained mechanism has one DOF, which is moving along the axis of the horizontal prismatic joint.

For the other section of the manipulator, namely, the parallel mechanism is a 3-PUU parallel mechanism having three translations with the axes of x , y , and z . So, the reconfigurable parallel manipulator needs four actuators to ensure it is working well.

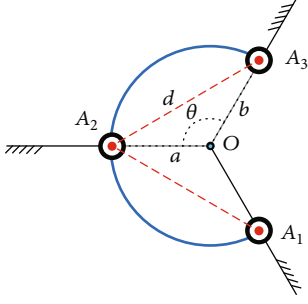


FIGURE 2: The schematic of the spatial multi-loop over-constrained mechanism.

2.3. Kinematic and Dynamic Analysis

2.3.1. The Kinematic of the Overconstrained Mechanism. The schematic of the spatial multiloop overconstrained mechanism is shown in Figure 2. The angles between any two links are all 120° . While for this mechanism, the input parameter is a , and the output parameter is b . The distance between any two links equals to d . Thus, based on the *cosine law*, the relationship between the input and output parameters can be written as

$$a^2 + b^2 - 2ab \cos(\theta) = d^2. \quad (6)$$

According to the actual application, the minus solution should be abandoned, so the result can be written as

$$b = \frac{-a + \sqrt{-3a^2 + 4d^2}}{2}. \quad (7)$$

2.3.2. Inverse Kinematic for the Parallel Mechanism. The schematic of the parallel mechanism is shown in Figure 3. The point, O , is the initial point attached to the ground and is represented by $Oxyz$. The local coordinates, $Ox_1y_1z_1$, is located at the central point of the moving platform. Their axial directions are shown in the following picture. As shown in Figure 3, $l_i (i=1, 2, 3)$ is the driving parameter and the output parameters are the coordinates of the O_1 . And l is the length of the fixed-length link, and a and b are the structural parameters obtained from Equation (7). The circumcircle radius of the moving platform is r .

For the inverse kinematic, it means the coordinates of point O_1 are known to solve the lengths of the driving joints, $l_i (i=1, 2, 3)$. In this paper, the proposed mechanism is symmetry, so the vector equation for each limb is similar. In this case, the closed-loop vector equation of the mechanism can be given as

$$\overrightarrow{OA_i} + \overrightarrow{A_iB_i} + \overrightarrow{B_iC_i} + \overrightarrow{C_iD_i} = \overrightarrow{OO_i} + \overrightarrow{O_iD_i} \quad (i=1, 2, 3). \quad (8)$$

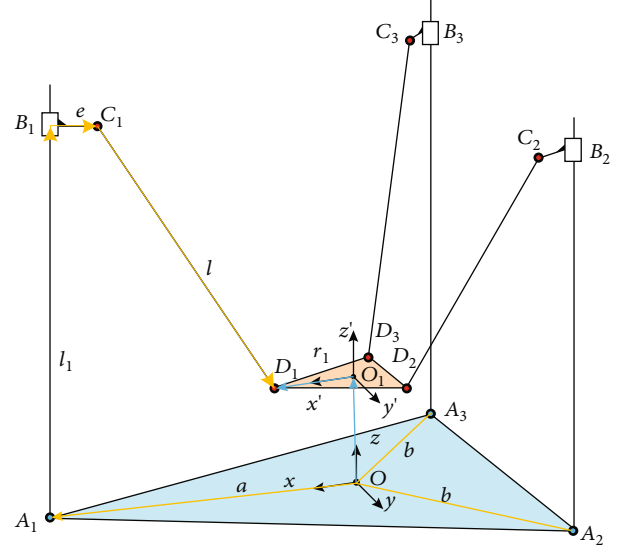


FIGURE 3: The schematic for the parallel mechanism.

The parallel mechanism only has three translations, so the rotation matrix from the local coordinate system to the fixed coordinate system is the unit matrix and the coordinates of the joints in each limb can be given as

$$\begin{aligned} \mathbf{C}_1 &= [a-f \quad 0 \quad l_1]^T; \\ \mathbf{D}_1 &= [x+r_1 \quad y \quad z]^T; \\ \mathbf{C}_2 &= \left[-\frac{b-f}{2} \quad \frac{-\sqrt{3}(b-f)}{2} \quad l_2 \right]^T; \\ \mathbf{D}_2 &= \left[x-\frac{r_1}{2} \quad y-\frac{\sqrt{3}r_1}{2} \quad z \right]^T; \\ \mathbf{C}_3 &= \left[-\frac{b-f}{2} \quad \frac{\sqrt{3}(b-f)}{2} \quad l_3 \right]^T; \\ \mathbf{D}_3 &= \left[x-\frac{r_1}{2} \quad y+\frac{\sqrt{3}r_1}{2} \quad z \right]^T. \end{aligned} \quad (9)$$

The coordinates of the central point of the moving platform located in the fixed coordinate system is $[x \quad y \quad z]^T$. Based on the structural constraints, the lengths of the fixed-length link are known, so the equation can be obtained as

$$\|\overrightarrow{C_iD_i}\| = l \quad (i=1, 2, 3). \quad (10)$$

Thus, the variables of the driving joints can be calculated by Equation (10).

2.4. Jacobian Matrix. For the parallel mechanisms, the Jacobian matrix is the mathematical basis to evaluate the performance of the mechanisms. In this paper, when the reconfigurable parallel mechanism is working, the configuration is determined, which means the reconfigurable mechanism is locked. The input parameters of the manipulator are only the lengths of three vertical prismatic joints, and the output parameters are the coordinates values of the central point located at the moving platform. Taking the time derivative of Equation (8) yields

$$\dot{\mathbf{l}}_i \times \overrightarrow{\mathbf{s}}_i + \overrightarrow{\mathbf{w}}_{ci} \times \overrightarrow{\mathbf{c}}_i = \dot{\mathbf{v}}_{o1} + \overrightarrow{\mathbf{w}}_{di} \times \overrightarrow{\mathbf{b}}_i, \quad (11)$$

where $\dot{\mathbf{l}}_i = [l_1 \ l_2 \ l_3]^T$ are the velocity of the driving joints, $\overrightarrow{\mathbf{s}}_i$ means the direction of the vertical prismatic joint, $\overrightarrow{\mathbf{w}}_{ci}$ is the angle velocity of the fixed-length link, $\overrightarrow{\mathbf{c}}_i$ is the vector of the fixed-length link, $\dot{\mathbf{v}}_{o1}$ is the velocity of the moving platform, $\overrightarrow{\mathbf{w}}_{di}$ is the angle velocity of the moving platform, and $\overrightarrow{\mathbf{b}}_i$ means the vector of $\overrightarrow{\mathbf{D}}_i\mathbf{O}_1$ in the local coordinate system.

Based on mathematical knowledge, simplifying Equation (11) yields

$$\begin{bmatrix} \dot{l}_1 \\ \dot{l}_2 \\ \dot{l}_3 \\ 0 \\ 0 \\ 0 \end{bmatrix} = \begin{bmatrix} \mathbf{c}_1 & \mathbf{c}_1 \times \mathbf{b}_1 \\ \mathbf{c}_2 & \mathbf{c}_2 \times \mathbf{b}_2 \\ \mathbf{c}_3 & \mathbf{c}_3 \times \mathbf{b}_3 \\ \mathbf{0} & \mathbf{s}_1 \\ \mathbf{0} & \mathbf{s}_2 \\ \mathbf{0} & \mathbf{s}_3 \end{bmatrix} \begin{bmatrix} v_x \\ v_y \\ v_z \\ w_x \\ w_y \\ w_z \end{bmatrix}. \quad (12)$$

Thus, the velocities of the three driving joints can be obtained, when the velocity of the moving platform is given.

2.5. Dynamic Analysis. In the industrial application, a dynamic model is an important section for the parallel mechanism. In this section, the inverse dynamic model is calculated for the parallel mechanism, based on the *Lagrangian Theory*. In general, there are several methods to obtain the dynamic model of the parallel mechanism, like *Lagrangian Theory*, *Newton-Euler Formulation*, and *Principle of Virtual Work*. In this paper, the proposed manipulator only has three translations, and the *Lagrangian Theory* is the best way for this manipulator to calculate this model.

For the proposed parallel mechanism, x , y , z , l_1 , l_2 , and l_3 are regarded as the generalized coordinates. The first type of Lagrangian equations can be written as

$$\frac{d}{dt} \left(\frac{\partial \mathbf{L}}{\partial \dot{\mathbf{q}}_j} \right) - \frac{\partial \mathbf{L}}{\partial \mathbf{q}_j} = \mathbf{Q}_j + \sum_{i=1}^k \lambda_i \frac{\partial \Gamma_i}{\partial \mathbf{q}_j} \quad (j = 1 \dots 6), \quad (13)$$

where Γ_i is the i^{th} constraint function, k is the number of constraint functions, and λ_i denotes the Lagrangian multiplier. \mathbf{Q}_j ($i = 1, 2, 3$) represent the x , y , and z components of an

external force exerted at the moving platform and \mathbf{Q}_j ($j = 4, 5, 6$) means the actuator force. L represents the total energy of the parallel mechanism.

The total energy includes kinetic energy and potential energy, and the kinetic energy can be given as

$$T = T_p + \sum_{i=1}^3 (T_{ai} + T_{bi}), \quad (14)$$

where T_p is the kinetic energy of the moving platform, T_{ai} is the kinetic energy of the vertical prismatic slider, and T_{bi} is the kinetic energy of the fixed-length link C_iD_i . In this paper, in order to simplify the dynamic model, assuming that the mass of each connecting rod, m_b , in the fixed-length link assembly is divided evenly and concentrated at the two end-points C_i and D_i . In this case, the kinetic energy of each part can be written as

$$\begin{aligned} T_p &= \frac{m_p(\dot{x}^2 + \dot{y}^2 + \dot{z}^2)}{2}, \\ T_{ai} &= \frac{m_a(\dot{l}_i)^2}{2}, \\ T_{bi} &= \frac{m_b(\dot{x}^2 + \dot{y}^2 + \dot{z}^2) + m_b(\dot{l}_i)^2}{2}, \end{aligned} \quad (15)$$

where m_a is the mass of the vertical prismatic slider.

The potential energy of the parallel mechanism can be written as

$$U = m_p g z + \sum_{i=1}^3 (m_a g l_i + m_b g (l_i + z)), \quad (16)$$

where g is the gravitational acceleration.

Based on Equations (14) and (16), the total energy of the parallel mechanism can be written as

$$\mathbf{L} = \mathbf{T} - \mathbf{U}. \quad (17)$$

Substituting the given variate into Equation (13), the λ_i can be calculated.

The second type of Lagrangian equations can be written as

$$\mathbf{F}_j = \frac{d}{dt} \left(\frac{\partial \mathbf{L}}{\partial \dot{\mathbf{q}}_j} \right) - \frac{\partial \mathbf{L}}{\partial \mathbf{q}_j} - \sum_{i=1}^k \lambda_i \frac{\partial \Gamma_i}{\partial \mathbf{q}_j} \quad (j = 1, 2, 3). \quad (18)$$

Thus, the input force F_j can be calculated.

3. Performance Analysis

3.1. Workspace. Workspace is the shape and volume that the manipulator can be reached in the global coordinate system. The constraints of the workspace include the structural parameters and the joint angle. In order to determine the

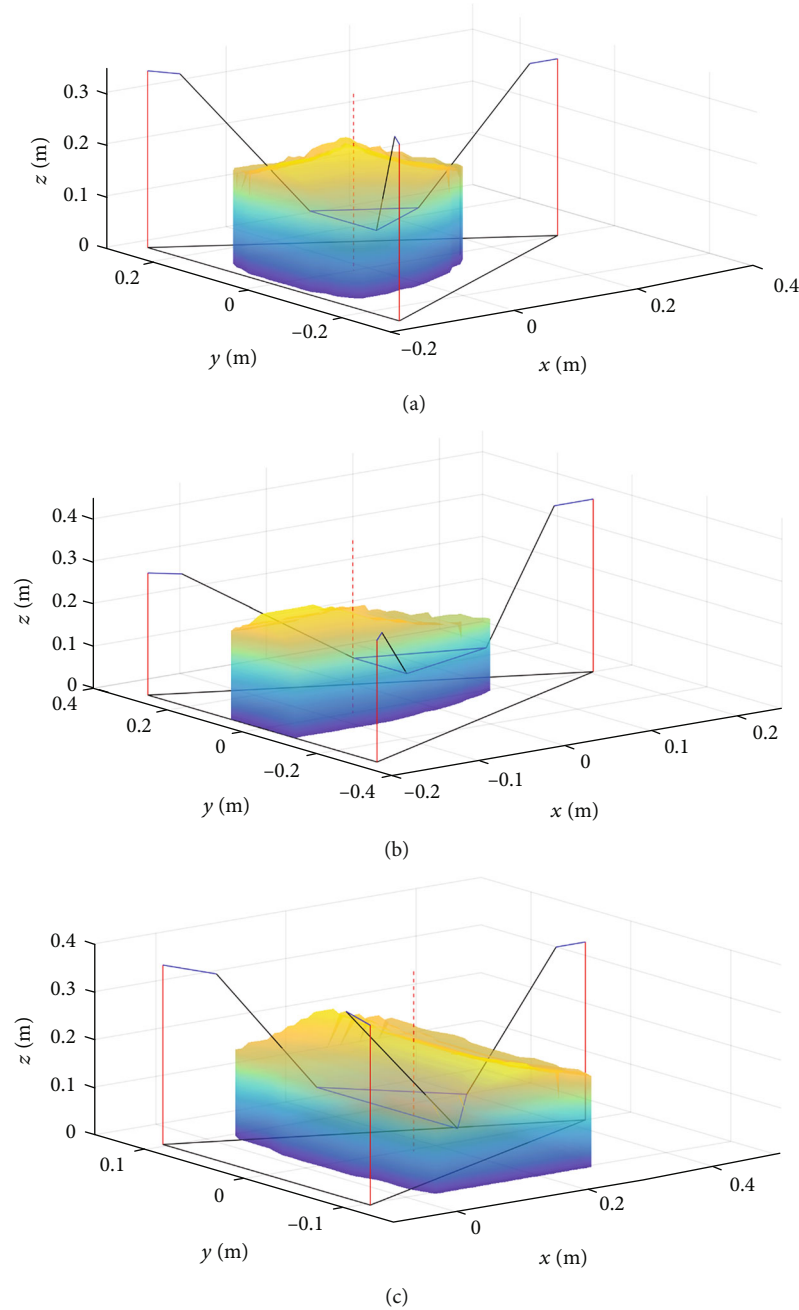


FIGURE 4: The workspace in different configurations.

workspace in the different configurations, the range of the driving joint is given as

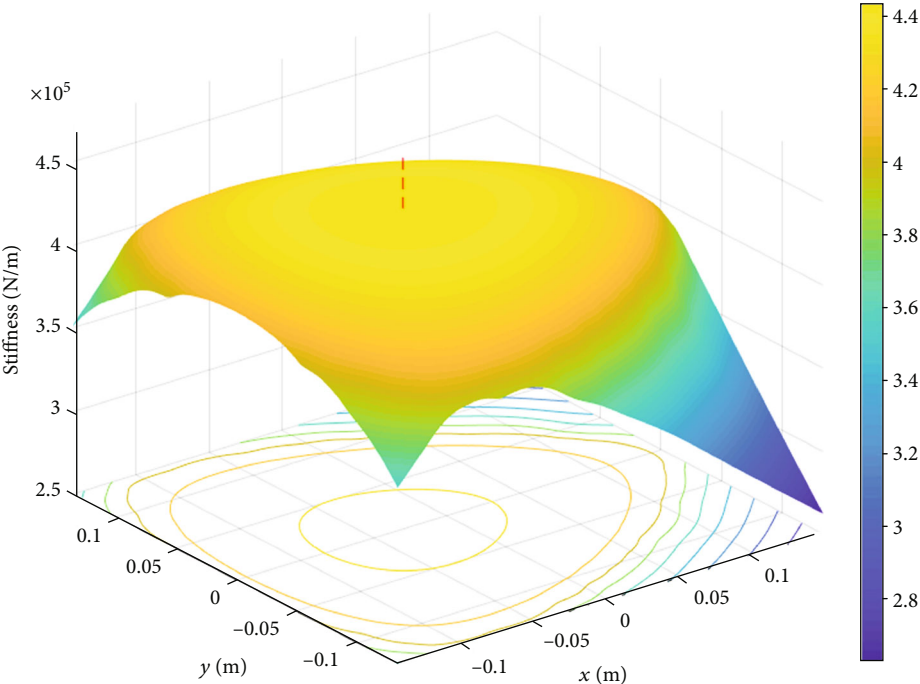
$$0.10 \text{ m} \leq l_i \leq 0.50 \text{ m} \quad (i = 1, 2, 3). \quad (19)$$

The range of the angle between the fixed-length link C_iD_i and the vertical prismatic joint A_iB_i is given as

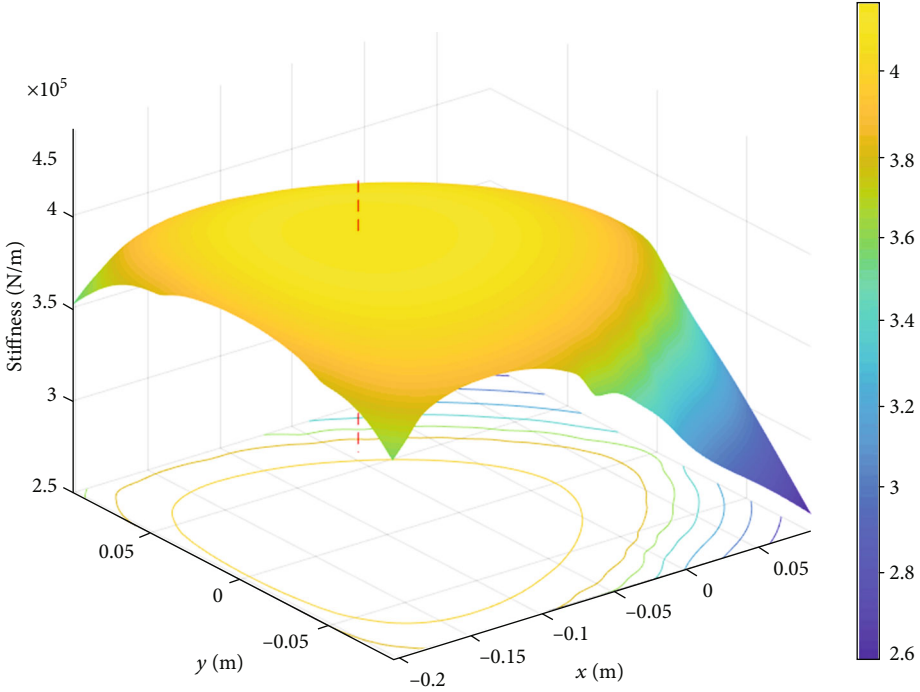
$$10^\circ \leq \beta_i \leq 75^\circ \quad (i = 1, 2, 3). \quad (20)$$

Thus, the figure of the workspace in different configurations is shown in Figure 4. Figure 4(a) shows the workspace

when $a = b$, which means the mechanism is central symmetry. And the workspace is also central symmetry seen from Figure 4(a). When $a = 0.25 \text{ m}$, the workspace is shown in Figure 4(b). When a is minimum, compared with Figure 4(a), the range of the workspace along y -axis is declining while the range along x -axis is increasing. The other limited situation is shown in Figure 4(c), namely, $a = 0.475 \text{ m}$. When a is maximum, the range of workspace along x -axis is declining while the range along y -axis is increasing. Thus, the proposed manipulator has a different workspace in different configurations, namely, this manipulator owns different performances in the aspect of workspace.



(a)



(b)

FIGURE 5: Continued.

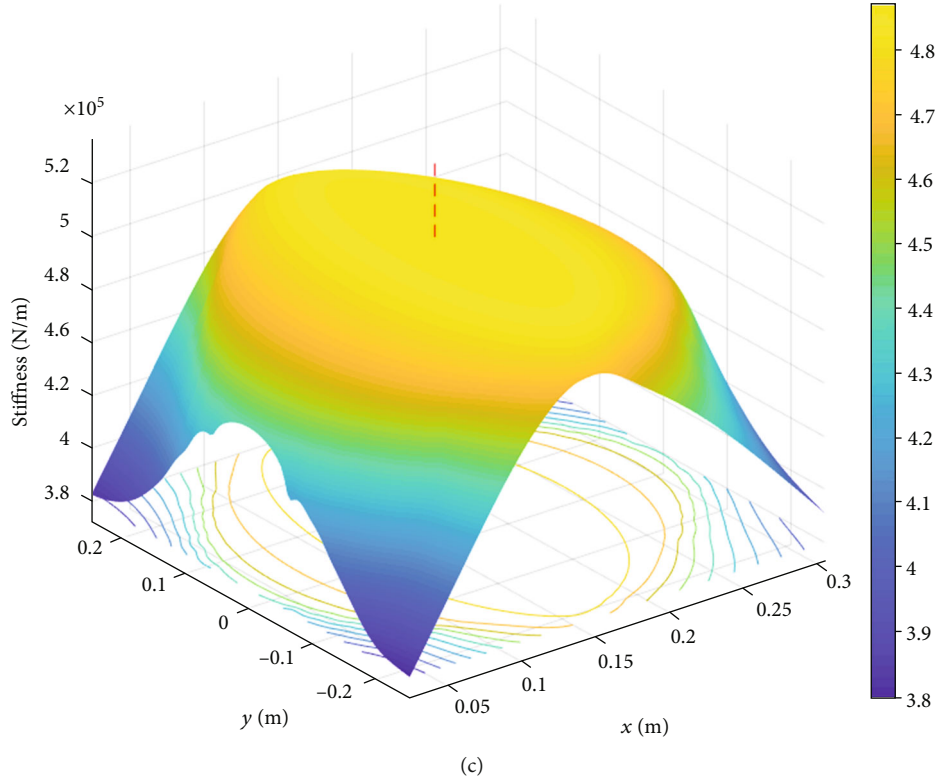


FIGURE 5: The stiffness in different configurations.

3.2. *Stiffness Analysis.* Stiffness is the deformation between the actual and desired position of the end effector, when the manipulator is given a task. To simplify the stiffness model, all the joints and links of this manipulator are regarded as rigid.

The stiffness of the manipulator is related to a wrench acting on the moving platform including the forces and moment. In this system, $\mathbf{w}_1 = [\mathbf{f}_1 \quad \mathbf{m}_1]^T$ is the wrench vector showing the forces and torques acting on the platform. In this vector, $\mathbf{f}_1 = [f_x \quad f_y \quad f_z]^T$ is the forces and $\mathbf{m}_1 = [m_x \quad m_y \quad m_z]^T$ represents the moments acting on the moving platform. For this parallel mechanism, both the constraint of structural configuration τ_c and the constraint of driving joints τ_a act on the manipulator. To balance the constraint forces or moments acting on the moving platform, the stiffness modeling of the manipulator can be written as

$$\mathbf{w}_1 = \mathbf{J}_a^{1T} \boldsymbol{\tau}_a^1 + \mathbf{J}_c^{1T} \boldsymbol{\tau}_c^1, \quad (21)$$

where

$$\boldsymbol{\tau}_a^1 = \boldsymbol{\chi}_a^1 \Delta \mathbf{q}_a^1, \quad (22)$$

$$\boldsymbol{\tau}_c^1 = \boldsymbol{\chi}_c^1 \Delta \mathbf{q}_c^1. \quad (23)$$

In Equation (22), $\Delta \mathbf{q}_a^1$ and $\Delta \mathbf{q}_c^1$ are representing the deformation of the actuators and structural configuration. And $\boldsymbol{\chi}_a^1 = \text{diag} [k_{a1}^1 \quad k_{a1}^2 \quad k_{a1}^3]$ and $\boldsymbol{\chi}_c^1 = \text{diag} [k_{c1}^1 \quad k_{c1}^2 \quad k_{c1}^3]$.

According to the *virtual work principle*, the equation of the manipulator can be given as

$$\mathbf{w}_1^T \Delta \mathbf{X}_1 = \boldsymbol{\tau}_a^{1T} \Delta \mathbf{q}_a^1 + \boldsymbol{\tau}_c^{1T} \Delta \mathbf{q}_c^1, \quad (24)$$

where $\Delta \mathbf{X}_1 = [\dot{x} \quad \dot{y} \quad \dot{z} \quad \dot{\theta}_x \quad \dot{\theta}_y \quad \dot{\theta}_z]^T$ is the deformation of the moving platform.

Combining Equations (21), (22), and (24), one can have

$$\mathbf{w}_1 = \mathbf{K}_1 \Delta \mathbf{X}_1, \quad (25)$$

where \mathbf{K}_1 is the generalized stiffness matrix which can be given as

$$\mathbf{K}_1 = \mathbf{J}_1^T \boldsymbol{\chi} \mathbf{J}_1, \quad (26)$$

$$\mathbf{J}_1 = \begin{bmatrix} \mathbf{c}_1 & \mathbf{c}_1 \times \mathbf{b}_1 \\ \mathbf{c}_2 & \mathbf{c}_2 \times \mathbf{b}_2 \\ \mathbf{c}_3 & \mathbf{c}_3 \times \mathbf{b}_3 \\ \mathbf{0} & \mathbf{s}_1 \\ \mathbf{0} & \mathbf{s}_2 \\ \mathbf{0} & \mathbf{s}_3 \end{bmatrix}. \quad (27)$$

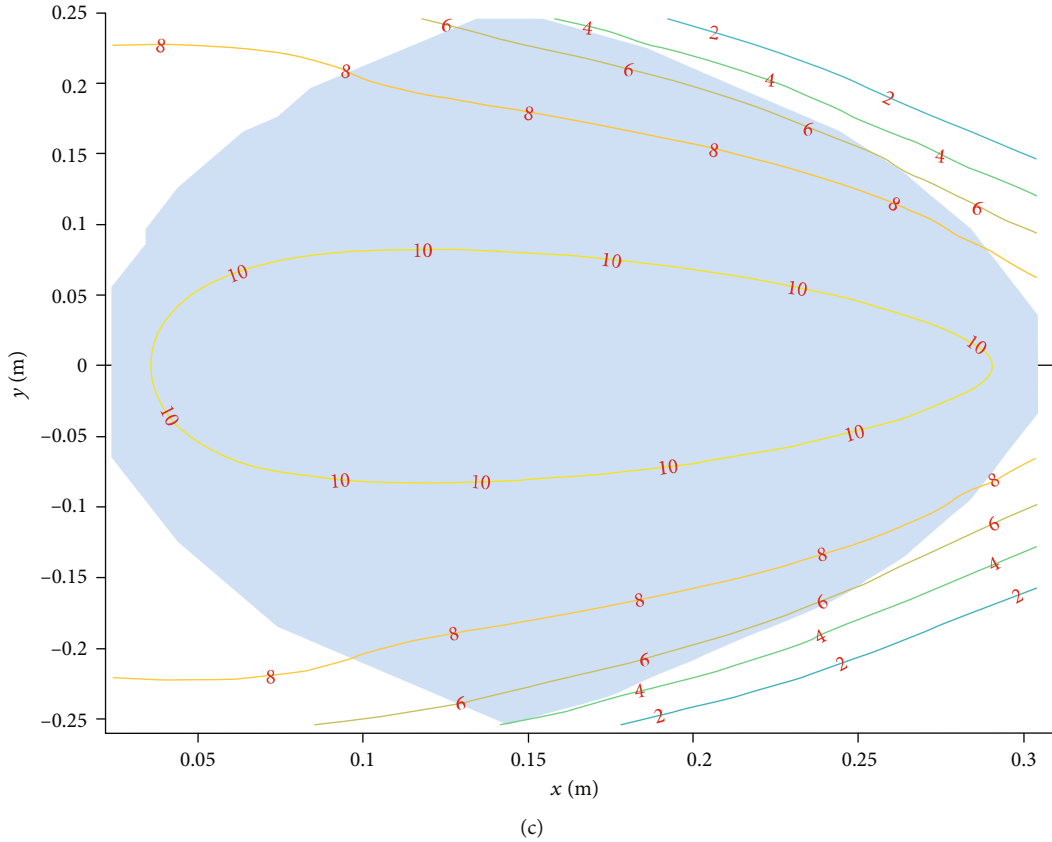


FIGURE 6: The condition number in different configurations.

Based on Equation (27), the stiffness can be expressed as

$$\begin{bmatrix} f_x \\ f_y \\ f_z \\ m_x \\ m_y \\ m_z \end{bmatrix} = \begin{bmatrix} k_{11} & k_{12} & k_{13} & k_{14} & k_{15} & k_{16} \\ k_{21} & k_{22} & k_{23} & k_{24} & k_{25} & k_{26} \\ k_{31} & k_{32} & k_{33} & k_{34} & k_{35} & k_{36} \\ k_{41} & k_{42} & k_{43} & k_{44} & k_{45} & k_{46} \\ k_{51} & k_{52} & k_{53} & k_{54} & k_{55} & k_{56} \\ k_{61} & k_{62} & k_{63} & k_{64} & k_{65} & k_{66} \end{bmatrix} \begin{bmatrix} \dot{x} \\ \dot{y} \\ \dot{z} \\ \dot{\theta}_x \\ \dot{\theta}_y \\ \dot{\theta}_z \end{bmatrix}. \quad (28)$$

Due to mobility analysis, the motions in θ_x , θ_y , and θ_z are constrained. Thus, the stiffness matrix can be rewritten as

$$\begin{bmatrix} f_x \\ f_y \\ f_z \end{bmatrix} = \begin{bmatrix} k_{11} & k_{12} & k_{13} \\ k_{21} & k_{22} & k_{23} \\ k_{31} & k_{32} & k_{33} \end{bmatrix} \begin{bmatrix} \dot{x} \\ \dot{y} \\ \dot{z} \end{bmatrix}. \quad (29)$$

In this paper, assuming $k_{ij} = 1 \times 10^6$ N/m ($i = 1, 2, 3; j = 1, 2, 3$) and $z = 0.15$ m, the stiffness of different configurations is shown in Figure 5. Figure 5(a) shows the stiffness of the manipulator when $a = b$. In this configuration, the mechanism is central symmetry and the mapping of the stiffness is symmetry, as well. When the end effector is closed to the cen-

tral area, the stiffness is maximum, which is about 4.5×10^5 N/m, while its stiffness is declining rapidly when the end effector is near the boundaries of the workspace. And the stiffness is declining more rapidly along the positive direction than the negative direction of x -axis. When $a = 0.25$ m, which means a is the minimum, the stiffness of the manipulator is shown in Figure 5(b). The distribution of stiffness is similar to Figure 5(a), but the central area is moving with negative x -axis, and the whole stiffness mapping figure moves about 0.05 m along the negative x -axis. The stiffness mapping along the y -axis is as symmetrical as when $a = b$. The stiffness of the manipulator is shown in Figure 5(c), when $a = 0.475$ m. Same as the above, near the central area, the manipulator has the highest stiffness and near the boundaries, the stiffness of the manipulator is declining. The acceptable stiffness range along the x -axis decreases, as well. However, the range along the y -axis becomes larger than $a = b$ and $a = 0.25$ m. And the shape of the mapping is the same as the mechanism's structure in this configuration. According to these figures, the manipulator has different performance in stiffness when the mechanism locates at different configurations, which means the manipulator owns reconfigurable ability.

4. Condition Number

Condition number is a performance to evaluate the dexterity of the manipulator, which is calculated from the Jacobian matrix. It can be given as

$$\kappa = \frac{\max(\text{eig}(J))}{\min(\text{eig}(J))}. \quad (30)$$

Based on Equation (30), the condition number is determined by the position of the end effector and $\kappa \geq 1$. When κ is closing to 1, the manipulator has the best dexterity. Figure 6 shows the condition number when $z = 0.15$ m in different configurations. When $a = b$, the condition number is shown in Figure 6(a). The shaded area is the projection of the workspace. The condition number range is from 1.45 to 1.85, which means the manipulator owns the balance performance in the workspace. Figure 6(b) shows the condition number when $a = 0.25$ m. In this configuration, the condition number is from 1.2 to 2. When the mechanism is locating at the boundary area, the mechanism has the better performance. When $a = 0.475$ m, the condition number is shown in Figure 6(c). The range is from 4 to 10, which means the mechanism has a significant difference in the workspace. And in this configuration, the mechanism owns worse performance than $a = b$ and $a = 0.25$ m in the aspect of dexterity. Although the condition number is not better, the range along the z -axis is increasing. Based on Figure 6, when $a = b$, the maximum condition number is 1.85, which is larger than the other two configurations. Thus, compared with another two cases, the manipulator has the best performance in condition number when $a = b$. According to the results, the manipulator has different performance in different configurations.

5. Neural Network and Its Application

5.1. Global Index. For the manipulator, condition number and stiffness are the performance located at a special point, not the global indices. In order to evaluate the performance in different configurations, the global indices about the stiffness and condition number should be proposed.

The global stiffness index (GSI) is given as

$$\text{GSI} = \frac{\int(\mathbf{K})dW}{\int dW}, \quad (31)$$

where $\int dW = \iiint dx dy dz$.

Similar to the GSI, the global condition number index (GCNI) can be given as

$$\text{GCNI} = \frac{\int(\kappa)dW}{\int dW}, \quad (32)$$

where $\int dW = \iiint dx dy dz$.

Besides the stiffness and condition number, the workspace is a global index. In this case, the performance for the manipulator in different configurations can be calculated. However, the units of the stiffness, condition number, and workspace are not identical; a method is proposed to solve

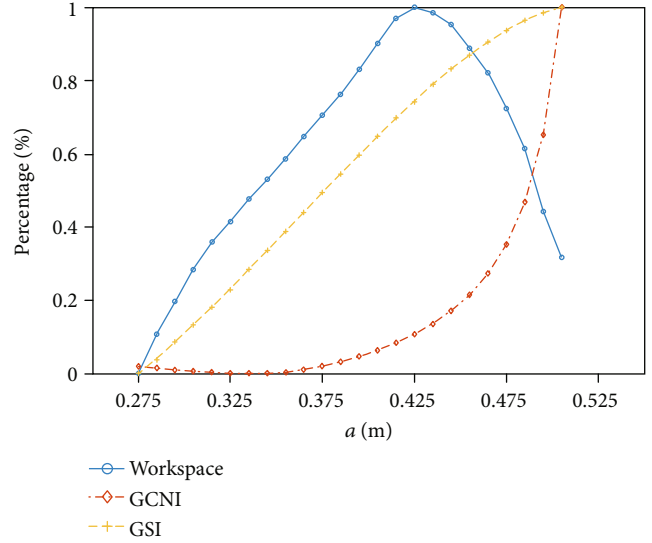


FIGURE 7: Trends of performance in different configurations.

this problem. This method can be written as

$$\tau = \frac{\eta_i - \min(\eta)}{\max(\eta) - \min(\eta)}. \quad (33)$$

In this paper, the range of the reconfigurable parameter, a , is $a \in [0.25 \text{ m}, 0.475 \text{ m}]$. Thus, the trend of these global indices is shown in Figure 7. As shown in Figure 7, when $a < 0.4$ m, the workspace is increasing with a , and when $a > 0.4$ m, the workspace is declining with a . The stiffness and condition number are both increasing with a . Thus, the manipulator has a different performance, when it is in a different configuration. Based on reconfigurable ability, the manipulator can be chosen as a suitable configuration for a certain requirement.

5.2. Performance Choice Based on a Neural Network. Traditionally, the performance of a special mechanism will be determined when the structural parameters are given. However, in the modern industrial area, based on the special task, determining the structural parameters becomes the tendency, especially for the reconfigurable parallel mechanism. In this paper, the modified *BP neural network* is used to solve this problem. Neural networks are noted for their extensive applications including pattern classification, function approximation, and optimization. The neural network includes BP neural network, RBF neural network, GRNN neural network, and Hopfield neural network.

BP neural network is a multilayer neural network, including an input layer, several hidden layers, and an output layer. Its remarkable character is that it is a feedback network and it can adjust its threshold and weight based on error backpropagation algorithm. Thus, in this paper, the BP neural network is the best choice to solve the above problem. According to the complex of these performance indices, a four-layer BP neural network is designed which means it has two hidden layers. The topology of the BP neural network

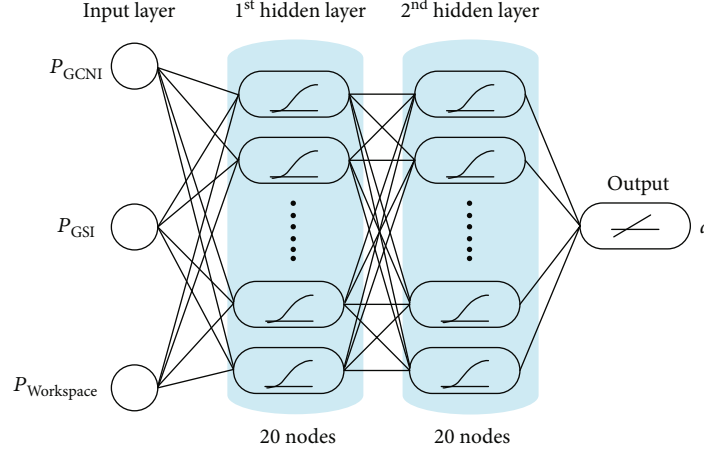


FIGURE 8: The topology of the BP neural network.

is shown in Figure 8. As shown in Figure 8, the input parameters are $[P_{GCNI} \ P_{GSI} \ P_{Workspace}]^T$ and the output parameter is the reconfigurable structural parameter, a . In order to obtain the accurate neural network, the hidden layers include two sections, and the functions of both sections are given as

$$f(x) = \frac{2}{1 + e^{-2x}} - 1. \quad (34)$$

In this case, the output of the note of the 1st hidden layer is given as

$$H_{j1} = f\left(\sum_{i=1}^n w_{ij1} x_{i1} - a_{j1}\right) \quad (j = 1, 2, \dots, 20), \quad (35)$$

where w_{ij1} is the weight between the input and the 1st hidden layers and a_{j1} is the threshold of the 1st hidden layer.

Similarly to Equation (35), the function between the 2nd hidden layer and the output layer is given as

$$H_{j2} = f\left(\sum_{i=1}^n w_{ij2} x_{i2} - a_{j2}\right) \quad (j = 1, 2, \dots, 20), \quad (36)$$

where w_{ij2} is the weight between 1st and 2nd hidden layers and a_{j2} is the threshold of the 2nd hidden layer.

The output of the output layer is given as

$$O = \sum_{j=1}^i H_{j2} w_j - b \quad (i = 1, 2, \dots, 20), \quad (37)$$

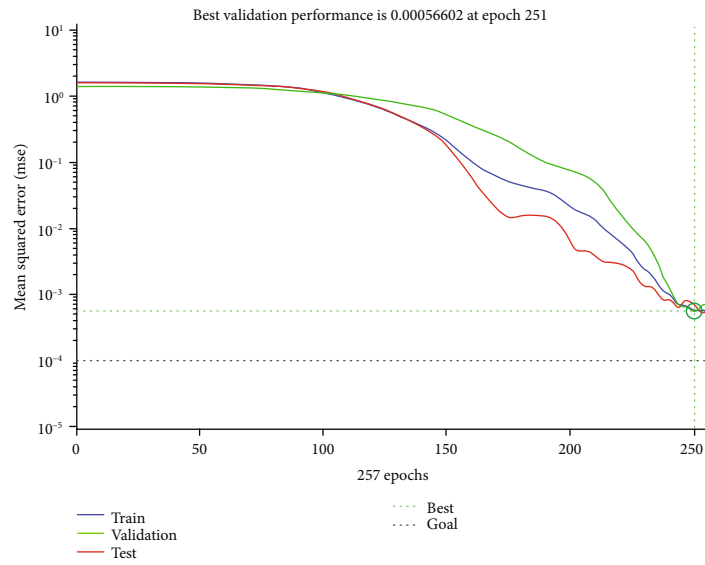
where w_j is the weight between 2nd hidden and output layers and b is the threshold of the output layer.

TABLE 1: The part of training samples.

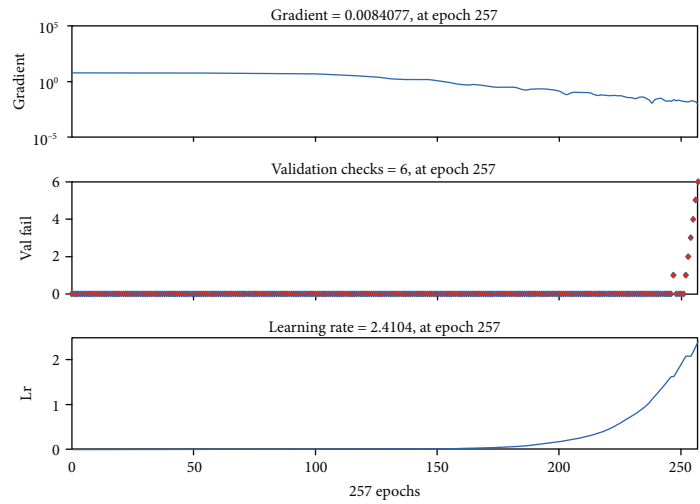
No.	Input parameters			Output parameters
	P_{GCNI}	P_{GSI}	$P_{Workspace}$	a (m)
1	0.0193	0.0000	0.0000	0.1250
2	0.0138	0.0380	0.1067	0.1350
3	0.0095	0.0870	0.1973	0.1450
4	0.0060	0.1324	0.2848	0.1550
5	0.0029	0.1812	0.3601	0.1650
6	0.0009	0.2287	0.4160	0.1750
7	0.0000	0.2849	0.4767	0.1850
8	0.0003	0.3360	0.5310	0.1950
9	0.0031	0.3878	0.5863	0.2050
10	0.0101	0.4400	0.6473	0.2150
11	0.0200	0.4939	0.7062	0.2250
12	0.0321	0.5453	0.7637	0.2350
13	0.0464	0.5965	0.8322	0.2450
14	0.0634	0.6484	0.9028	0.2550
15	0.0835	0.6993	0.9706	0.2650
16	0.1066	0.7428	1.0000	0.2750
17	0.1358	0.7909	0.9855	0.2850
18	0.1709	0.8330	0.9545	0.2950
19	0.2147	0.8698	0.8893	0.3050
20	0.2734	0.9062	0.8221	0.3150
21	0.3527	0.9383	0.7241	0.3250
22	0.4683	0.9651	0.6140	0.3350
23	0.6533	0.9857	0.4424	0.3450
24	1.0000	1.0000	0.3175	0.3550

The error between actual output, O , and desired output, Y is given as

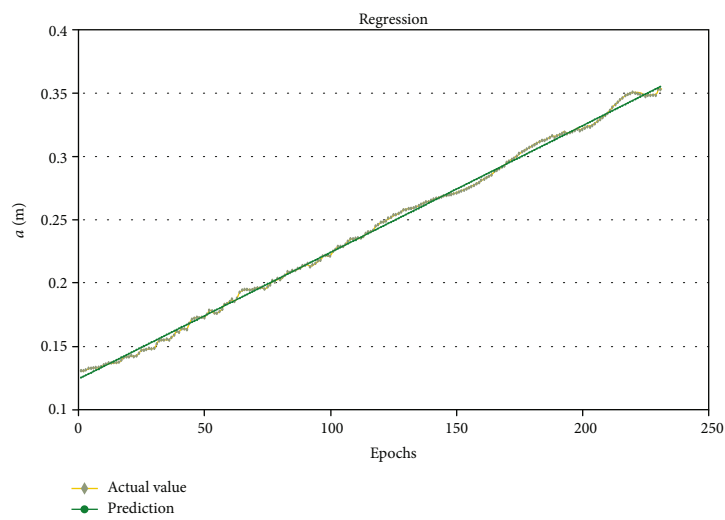
$$e = \frac{1}{2}(O - Y)^2. \quad (38)$$



(a)



(b)



(c)

FIGURE 9: The results of the trained neural network.

TABLE 2: The test and actual indices.

Desired indices				Actual indices		
P_{GCNI}	P_{GSI}	$P_{Workspace}$	a (m)	P_{GCNI}	P_{GSI}	$P_{Workspace}$
0.0137	0.0444	0.1155	0.1364	0.0134	0.0457	0.1147
0.0140	0.4637	0.6628	0.2173	0.0125	0.4561	0.6474
0.2480	0.8925	0.8567	0.3148	0.2721	0.9057	0.8206
0.8311	0.9951	0.3815	0.3481	0.7367	0.9913	0.4405
0.1390	0.7946	0.9851	0.2831	0.1301	0.7825	0.9935
0.0011	0.2287	0.4143	0.1749	0.0011	0.2287	0.4147
0.0006	0.3406	0.5320	0.1962	0.0006	0.3420	0.533
0.0548	0.6217	0.8642	0.2538	0.0616	0.6428	0.8908
0.3348	0.9324	0.7214	0.3201	0.3108	0.9239	0.774

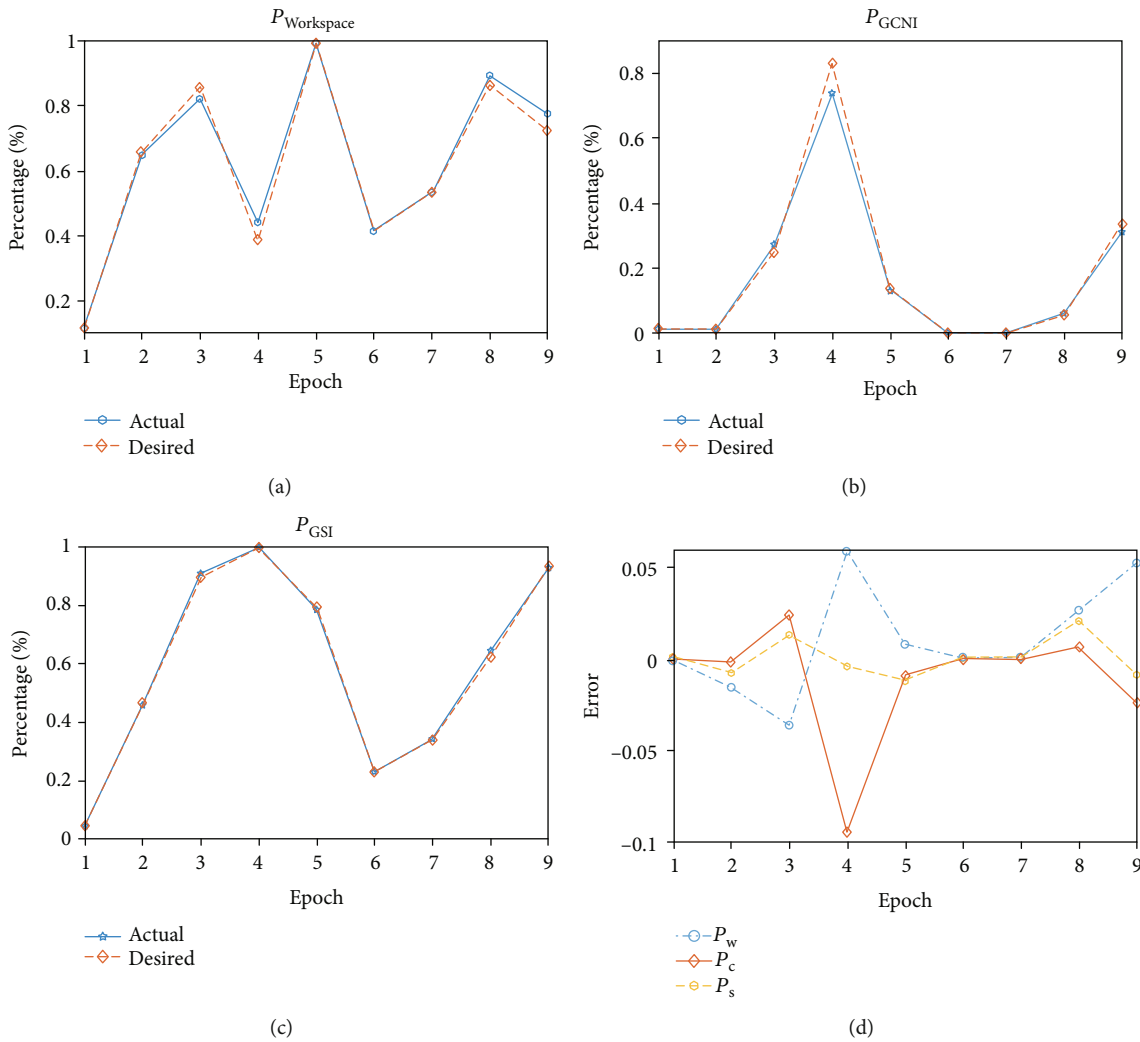


FIGURE 10: The comparison between actual and desired indices.

In order to obtain the best weight and threshold faster, the additional momentum method is applied, which can be given as

$$w(k) = w(k-1) + \Delta w(k) + a[w(k-1) - w(k-2)], \quad (39)$$

where $w(k)$, $w(k-1)$, and $w(k-2)$ are the weight at time k , $k-1$, and $k-2$, separately.

At the same time, the variable learning method is used to make the training process faster, which is given as

TABLE 3: The structural and dynamic parameters.

Parameter	Value	Parameter	Value	Parameter	Value	Parameter	Value
m_a	0.4799 kg	m_b	0.1323 kg	f_y	0 N	f_z	0 N
m_p	1.5750 m	f_x	0 N	a_x	0 m/s ²	a_y	0 m/s ²
a_z	0 m/s ²	a	0.307 m	l	0.331 m	r	0.01 m
e	0.045 m	r_1	0.081 m				

$$\eta(t+1) = \begin{cases} k_{\text{inc}}\eta(t)E(t+1) < E(t), \\ k_{\text{dec}}\eta(t)E(t+1) > E(t), \\ \eta(t)E(t+1) = E(t), \end{cases} \quad (40)$$

where k is the learning rate. Generally, $k_{\text{inc}} > 1$ and $0 < k_{\text{dec}} < 1$.

In this paper, part of all training samples is listed in Table 1. There are 24 samples in the table; however, 24 samples are too little to train the neural network. In this paper, 241 samples are used to train the BP neural network. Then, the trained neural network is obtained. Figure 9 shows the result of the trained neural network. Figure 9(a) is the error of the neural network, and in 257th epoch, the neural network is trained well, which has the best performance. Figure 9(b) shows the gradient, validation, and learning rate in the training process, separately. Figure 9(c) shows the regression between the actual training samples and output parameters.

Some random tasks are presented to verify the effectiveness of the neural network. Firstly, these desired indices are put into the input layer of the neural network; then, the reconfigurable parameter, a , can be calculated by the neural network. Next, the calculated parameters are substituted into the kinematic model, while the actual indices can be obtained. Finally, comparing the desired and actual indices, the effectiveness of the neural network can be verified. These indices are listed in Table 2. Figure 10 shows the comparison between the desired and actual indices. Figures 10(a)–10(c) show the $P_{\text{Workspace}}$, P_{GCNI} , and P_{GSI} between the actual and desired indices, separately. Figure 10(d) shows these indices of error between actual and desired indices. Compared with the desired indices, these errors can be neglected. Thus, the trained neural network can obtain the reconfigurable parameter well and work well. Based on the trained neural network, the configuration can be determined, according to the requirement of a certain task.

6. Numerical Example

In this section, a special task is presented to verify the correctness of kinematic and dynamic models. In this sample, the external forces are all zero and the initial position of the central point is $[0 \ 0 \ 0.1]^T$. The structural and mass parameters are listed in Table 3.

The equation of the end effector's trajectory is given as

$$\begin{cases} r_a = u(n+t), \\ x = r_a \cos(t), \\ y = r_a \sin(t), \\ z = 0.1, \end{cases} \quad (41)$$

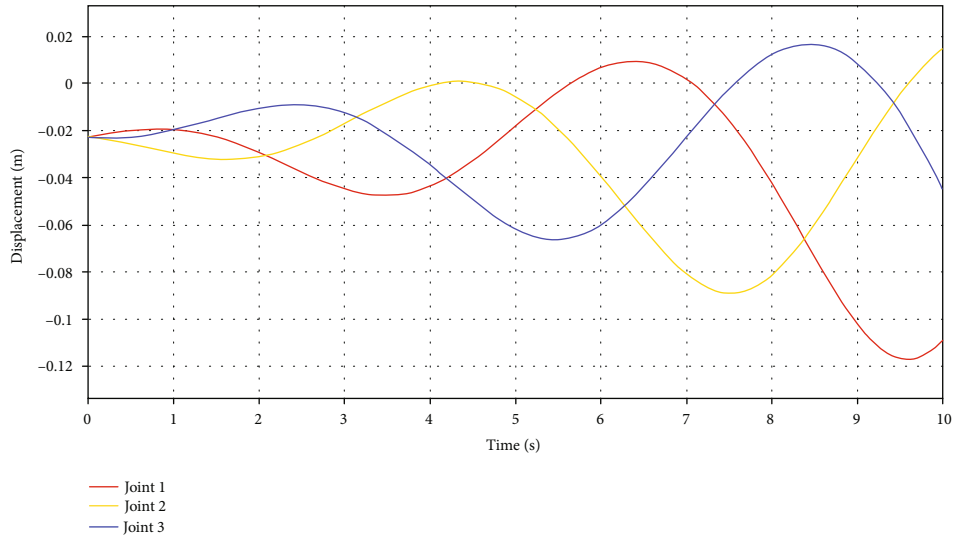
where t is the time, r is the radius of the curve, and z_1 is the value along the z -axis. In this sample, $t = 10$ s, $z_1 = 0.1$ m, $u = 0.01$ m, and $n = 0.01$ s. And the result is shown in Figure 11.

As shown in Figure 11, Figure 11(a) is the actual trend of driving joints, which is obtained from the simulation soft. (b) is the desired length of the joints, which is calculated by the kinematic model. (c) shows the errors between actual and desired joints and the error is very small. (d) is the error along the z -axis. (e) is the error between the actual and desired trajectory in the plane. From these figures, the error exists, but it is very small, and it can be neglectful. Thus, the inverse kinematic model can be verified.

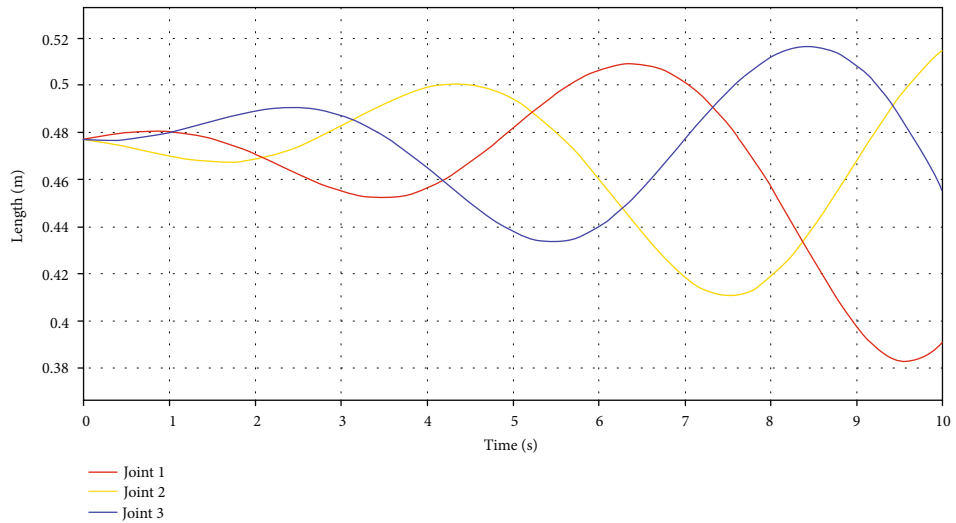
The dynamic result is shown in Figure 12. Figure 12(a) shows the accelerations of three joints when the trajectory of the end effector is the Archimedes spiral. (b) is the driving force of these joints. According to Figures 12(a) and 12(b), the tendency of accelerations and driving forces is similar, which confirms to reality. Figures 12(c)–12(e) are the mapping of the driving forces along the x, y -axis, separately. Along different directions, the different driving forces are increasing, monotonously.

7. Conclusion

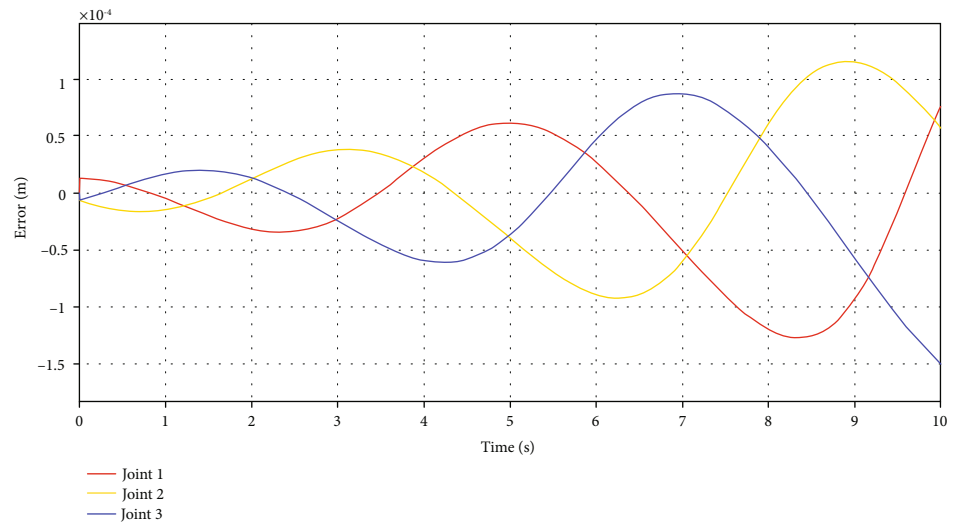
This paper presents a novel reconfigurable parallel mechanism based on the spatial multiloop overconstrained mechanism. According to the screw theory, the mobility of the reconfigurable is analyzed. The reconfigurable mechanism has one DOF, and it can change the parallel mechanism's structural parameter. Then, the performance of the reconfigurable parallel mechanism will be changed. The inverse kinematic and dynamic model of the reconfigurable parallel mechanism are both established. Thus, based on the Jacobian Matrix, some performance indices are proposed. And the different performances in different configurations are analyzed. And it shows that the novel



(a)

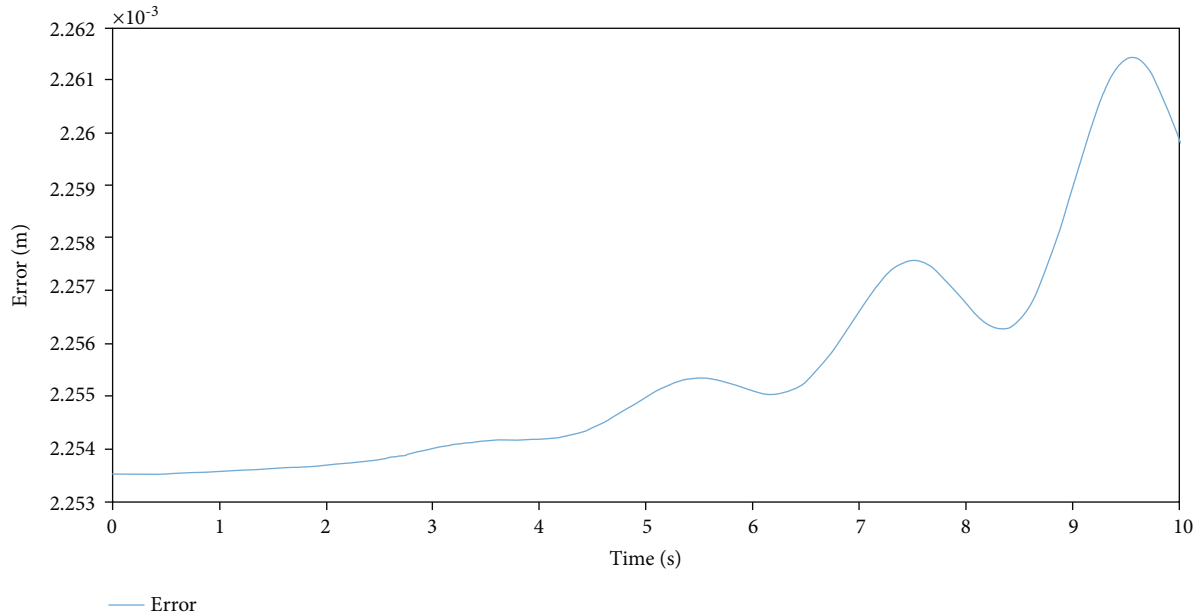


(b)

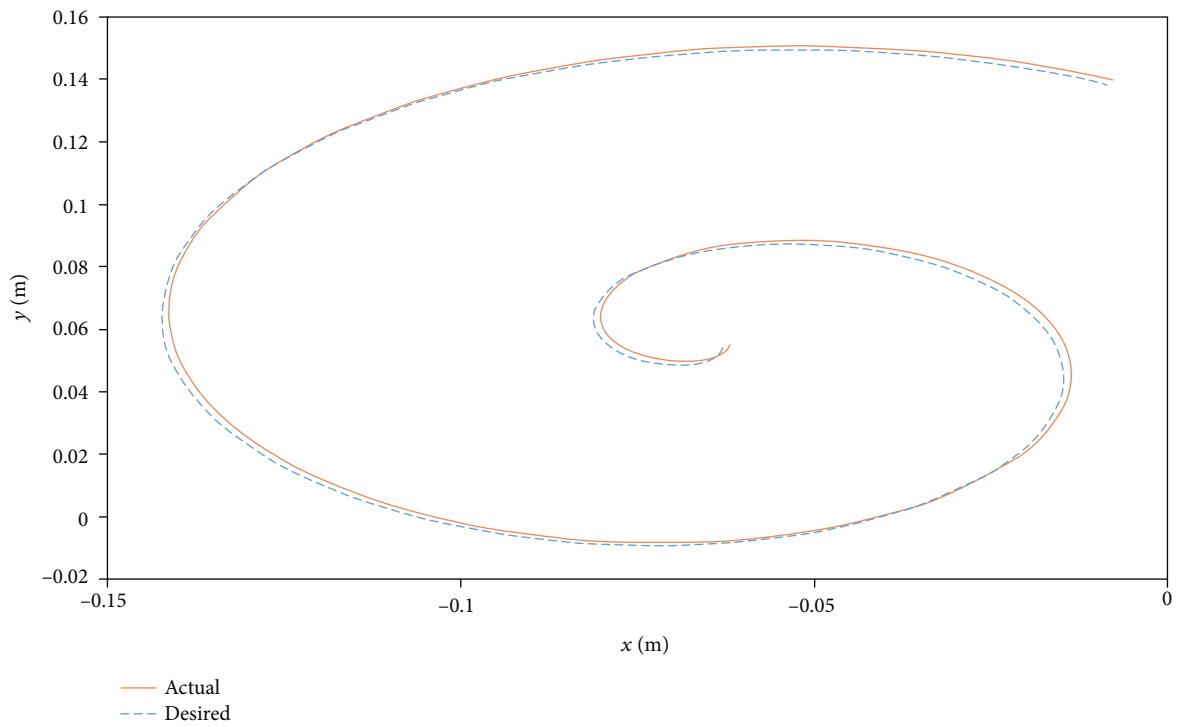


(c)

FIGURE 11: Continued.



(d)

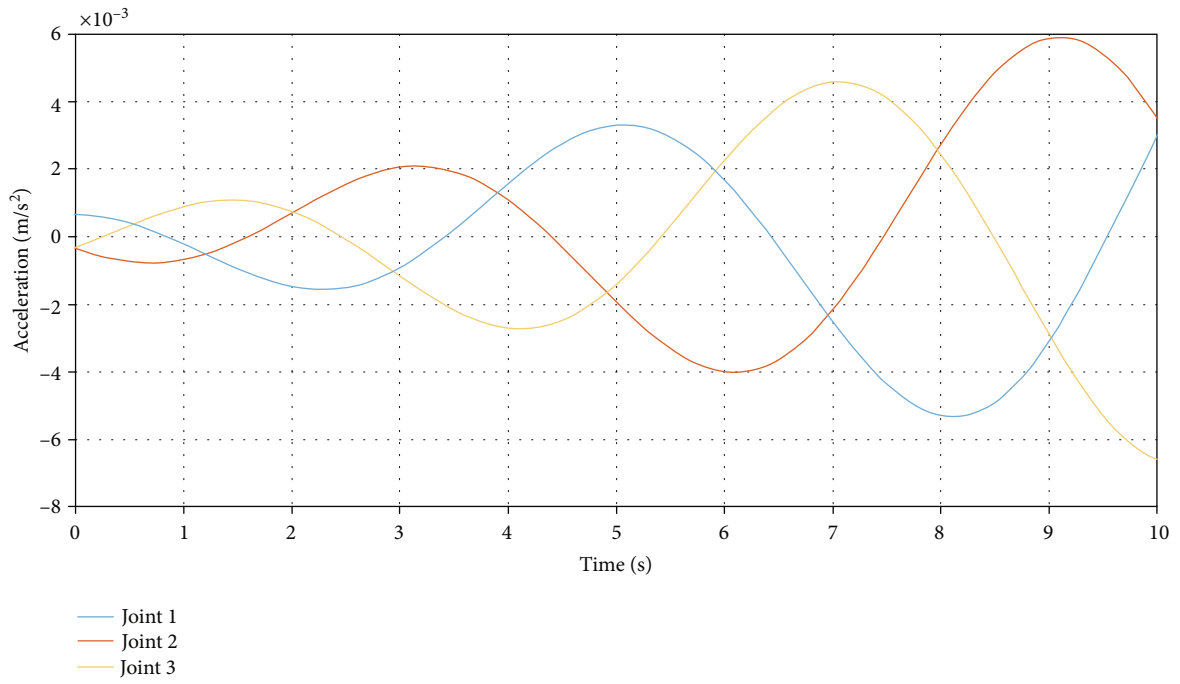


(e)

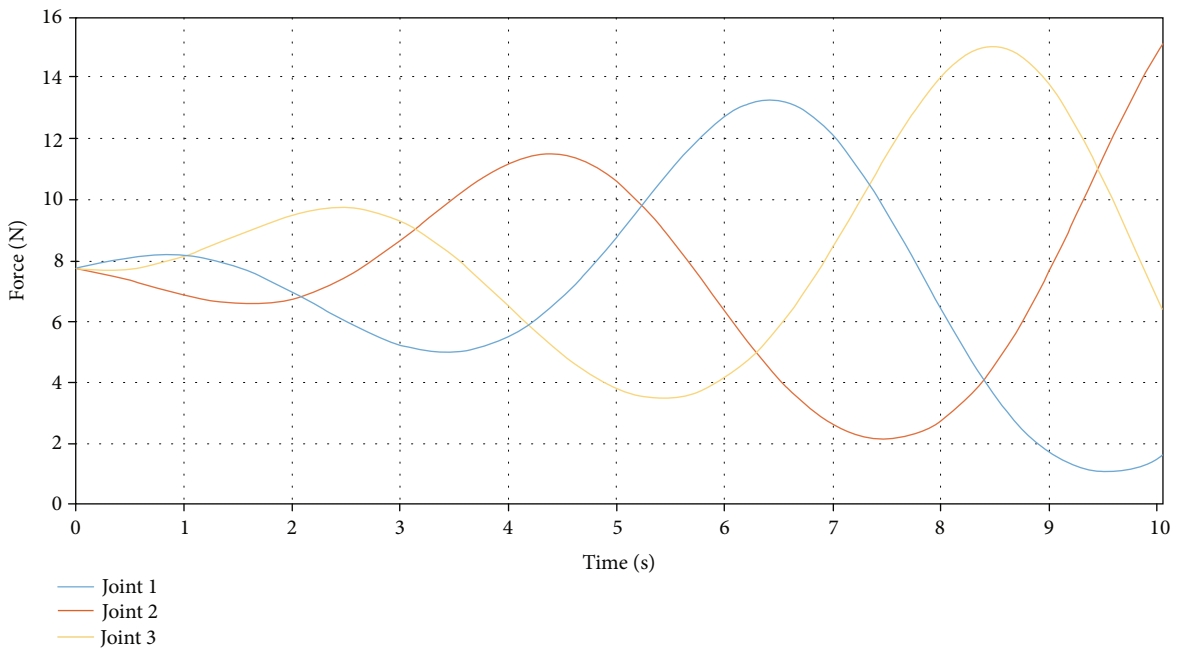
FIGURE 11: The result of simulation.

reconfigurable parallel mechanism has some configurations and the reconfigurable parallel mechanism has different performance indices. In order to choose the best configuration based on the special task requirement, by using the modified BP neural network, an algorithm is designed to solve this problem. And some samples are used to train the algorithm. Then, based on the trained

neural network, some test samples are proposed to verify the correctness and accuracy of the designed neural network. Thus, a suitable configuration can be determined by the special requirement in the industrial area. Finally, based on a certain task, the numerical example is proposed to verify the correctness of the inverse kinematic and dynamic models.

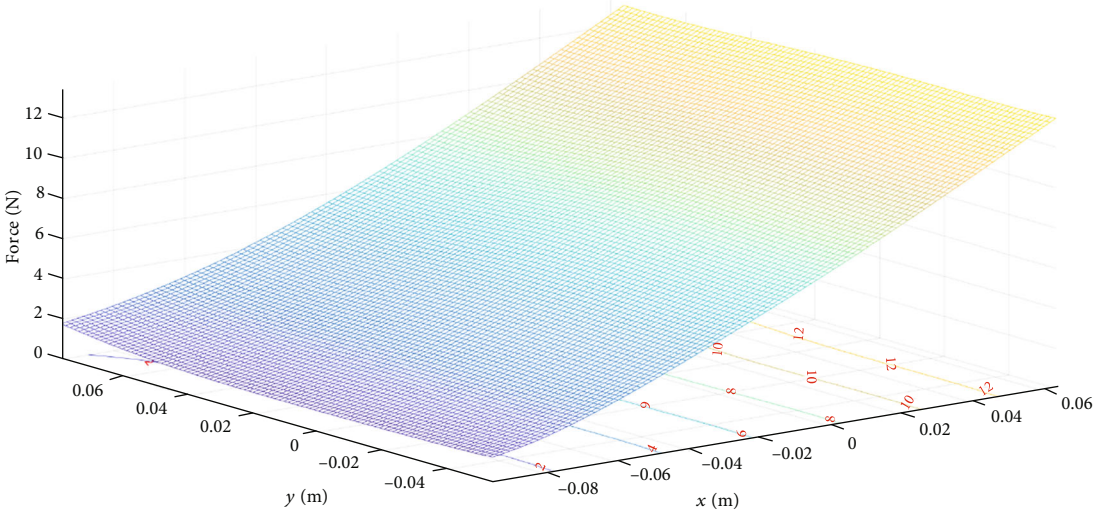


(a)

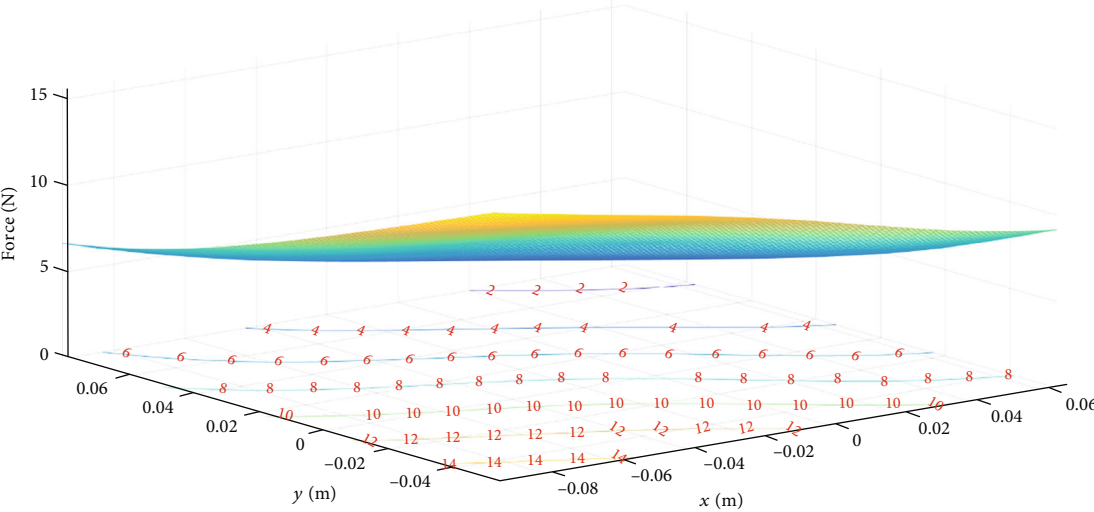


(b)

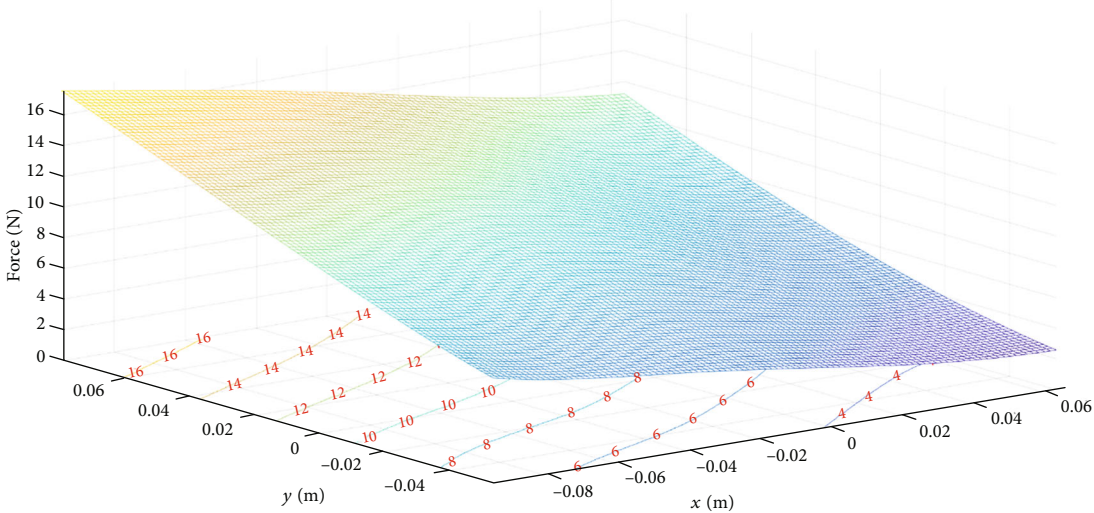
FIGURE 12: Continued.



(c)



(d)



(e)

FIGURE 12: The result of dynamic simulation.

Data Availability

The MATLAB code and the data used to support the findings of this study are available from the first author upon request.

Conflicts of Interest

The authors declared no potential conflicts of interest with respect to the research, authorship, and/or publication of this article.

Acknowledgments

The 1st author would like to thank the financial support from the Youth Foundation of Zhejiang Lab (Grant No. 2020NB0AA02) and the Leading Innovation and Entrepreneurship Team of Zhejiang Province of China (Grant No. 2018R01006). The 1st, 2nd, and 3rd authors would like to thank the financial support from the Natural Sciences and Engineering Research Council of Canada (NSERC) and gratefully acknowledge the financial support from the York Research Chairs (YRC) program.

References

- [1] W. Ye, Y. Fang, and S. Guo, "Design and analysis of a reconfigurable parallel mechanism for multidirectional additive manufacturing," *Mechanism and Machine Theory*, vol. 112, pp. 307–326, 2017.
- [2] G. Huang, S. Guo, D. Zhang, H. Qu, and H. Tang, "Kinematic analysis and multi-objective optimization of a new reconfigurable parallel mechanism with high stiffness," *Robotica*, vol. 36, no. 2, pp. 187–203, 2018.
- [3] G. Huang, D. Zhang, S. Guo, and H. Qu, "Design and optimization of a novel three-dimensional force sensor with parallel structure," *Sensors*, vol. 18, no. 8, article 2416, 2018.
- [4] W. Ye and Q. Li, "Type synthesis of lower mobility parallel mechanisms: a review," *Chinese Journal of Mechanical Engineering*, vol. 32, no. 1, p. 38, 2019.
- [5] M. Li, T. Huang, D. Zhang, X. Zhao, S. J. Hu, and D. G. Chetwynd, "Conceptual design and dimensional synthesis of a reconfigurable hybrid robot," *Journal of Manufacturing Science and Engineering*, vol. 127, no. 3, pp. 647–653, 2005.
- [6] F. Xi, Y. Xu, and G. Xiong, "Design and analysis of a reconfigurable parallel robot," *Mechanism and Machine Theory*, vol. 41, no. 2, pp. 191–211, 2006.
- [7] R. Fisher, R. P. Podhorodeski, and S. B. Nokleby, "Design of a reconfigurable planar parallel manipulator," *Journal of Robotic Systems*, vol. 21, no. 12, pp. 665–675, 2004.
- [8] K. Zhang and J. S. Dai, "Screw-system-variation enabled reconfiguration of the Bennett plano-spherical hybrid linkage and its evolved parallel mechanism," *Journal of Mechanical Design*, vol. 137, no. 6, p. 62303, 2015.
- [9] D. Gan, J. Dias, and L. Seneviratne, "Unified kinematics and optimal design of a 3rR PS metamorphic parallel mechanism with a reconfigurable revolute joint," *Mechanism and Machine Theory*, vol. 96, pp. 239–254, 2016.
- [10] W. Ye, X. Chai, and K. Zhang, "Kinematic modeling and optimization of a new reconfigurable parallel mechanism," *Mechanism and Machine Theory*, vol. 149, article 103850, 2020.
- [11] W. Ye, Y. Fang, K. Zhang, and S. Guo, "Mobility variation of a family of metamorphic parallel mechanisms with reconfigurable hybrid limbs," *Robotics and Computer-Integrated Manufacturing*, vol. 41, pp. 145–162, 2016.
- [12] W. Ye, Y. Fang, K. Zhang, and S. Guo, "A new family of reconfigurable parallel mechanisms with diamond kinematotropic chain," *Mechanism and Machine Theory*, vol. 74, pp. 1–9, 2014.
- [13] K. Zhang, J. S. Dai, and Y. Fang, "Geometric constraint and mobility variation of two 3S_vps_v metamorphic parallel mechanisms," *Journal of Mechanical Design*, vol. 135, no. 1, 2013.
- [14] D. Gan, J. S. Dai, J. Dias, and L. Seneviratne, "Constraint-plane-based synthesis and topology variation of a class of metamorphic parallel mechanisms," *Journal of Mechanical Science and Technology*, vol. 28, no. 10, pp. 4179–4191, 2014.
- [15] Y. Zhuang and D. Gan, "Unified singularity modeling and reconfiguration of 3rTPSMetamorphic parallel mechanisms with parallel constraint screws," *Advances in Mechanical Engineering*, vol. 7, no. 2, Article ID 352797, 2014.
- [16] D. Gan, J. S. Dai, J. Dias, and L. Seneviratne, "Reconfigurability and unified kinematics modeling of a 3rTPS metamorphic parallel mechanism with perpendicular constraint screws," *Robotics and Computer-Integrated Manufacturing*, vol. 29, no. 4, pp. 121–128, 2013.
- [17] X. J. Liu, J. Li, and Y. Zhou, "Kinematic optimal design of a 2-degree-of-freedom 3-parallel-gram planar parallel manipulator," *Mechanism and Machine Theory*, vol. 87, pp. 1–17, 2015.
- [18] S. Herrero, T. Mannheim, I. Prause, C. Pinto, B. Corves, and O. Altuzarra, "Enhancing the useful workspace of a reconfigurable parallel manipulator by grasp point optimization," *Robotics and Computer-Integrated Manufacturing*, vol. 31, pp. 51–60, 2015.
- [19] H. Zhang, H. Fang, Y. Fang, and B. Jiang, "Workspace analysis of a hybrid kinematic machine tool with high rotational applications," *Mathematical Problems in Engineering*, vol. 2018, Article ID 2607497, 12 pages, 2018.
- [20] W. Ye, L. He, and Q. Li, "A new family of symmetrical 2T2R parallel mechanisms without parasitic motion," *Journal of Mechanisms and Robotics*, vol. 10, no. 1, article 011006, 2018.
- [21] A. Klimchik, D. Chablat, and A. Pashkevich, "Stiffness modeling for perfect and non-perfect parallel manipulators under internal and external loadings," *Mechanism and Machine Theory*, vol. 79, pp. 1–28, 2014.
- [22] R. A. Srivatsan and S. Bandyopadhyay, "On the position kinematic analysis of MaPaMan: a reconfigurable three-degrees-of-freedom spatial parallel manipulator," *Mechanism and Machine Theory*, vol. 62, pp. 150–165, 2013.
- [23] F. Zhao, S. Guo, C. Zhang, H. Qu, and D. Li, "Singularity analysis and dexterity performance on a novel parallel mechanism with kinematic redundancy," *International Journal of Advanced Robotic Systems*, vol. 16, no. 5, 2019.
- [24] J. Li, L. Zhang, M. Dong, S. Zuo, Y. He, and P. Zhang, "Velocity and force transfer performance analysis of a parallel hip assistive mechanism," *Robotica*, vol. 38, no. 4, pp. 747–759, 2020.
- [25] G. Coppola, D. Zhang, and K. Liu, "A 6-Dof reconfigurable hybrid parallel manipulator," *Robotics and Computer-Integrated Manufacturing*, vol. 30, no. 2, pp. 99–106, 2014.
- [26] T. Huang, M. Li, X. M. Zhao, J. P. Mei, D. G. Chetwynd, and S. J. Hu, "Conceptual design and dimensional synthesis for a 3-Dof module of the Trivariant-a novel 5-Dof reconfigurable

- hybrid robot,” *IEEE Transactions on Robotics*, vol. 21, no. 3, pp. 449–456, 2005.
- [27] J. Wang, C. Wu, and X. J. Liu, “Performance evaluation of parallel manipulators: motion/force transmissibility and its index,” *Mechanism and Machine Theory*, vol. 45, no. 10, pp. 1462–1476, 2010.
- [28] G. Huang, D. Zhang, S. Guo, and H. Qu, “Structural synthesis of a class of reconfigurable parallel manipulators based on over-constrained mechanisms,” *International Journal of Robotics and Automation*, vol. 34, no. 2, 2019.
- [29] C. Brisan and A. Csiszar, “Computation and analysis of the workspace of a reconfigurable parallel robotic system,” *Mechanism and Machine Theory*, vol. 46, no. 11, pp. 1647–1668, 2011.
- [30] C. Viegas, M. Tavakoli, and A. T. Almeida, “A novel grid-based reconfigurable spatial parallel mechanism with large workspace,” *Mechanism and Machine Theory*, vol. 115, pp. 149–167, 2017.
- [31] C. T. Chen, “Reconfiguration of a parallel kinematic manipulator for the maximum dynamic load-carrying capacity,” *Mechanism and Machine Theory*, vol. 54, pp. 62–75, 2012.
- [32] Z. Gao and D. Zhang, “Performance analysis, mapping, and multi-objective optimization of a hybrid robotic machine tool,” *IEEE Transactions on Industrial Electronics*, vol. 62, no. 1, pp. 423–433, 2015.
- [33] Z. Chi and D. Zhang, “Stiffness optimization of a novel reconfigurable parallel kinematic manipulator,” *Robotica*, vol. 30, no. 3, pp. 433–447, 2012.
- [34] W. Ye, B. Zhang, and Q. Li, “Design of a 1R1T planar mechanism with remote center of motion,” *Mechanism and Machine Theory*, vol. 149, p. 103845, 2020.
- [35] D. Zhang and J. Lei, “Kinematic analysis of a novel 3-Dof actuation redundant parallel manipulator using artificial intelligence approach,” *Robotics and Computer-Integrated Manufacturing*, vol. 27, no. 1, pp. 157–163, 2011.
- [36] D. Zhang and Z. Gao, “Forward kinematics, performance analysis, and multi-objective optimization of a bio-inspired parallel manipulator,” *Robotics and Computer-Integrated Manufacturing*, vol. 28, no. 4, pp. 484–492, 2012.
- [37] F. Bourbonnais, P. Bigras, and I. A. Bonev, “Minimum-time trajectory planning and control of a pick-and-place five-bar parallel robot,” *IEEE/ASME Transactions on Mechatronics*, vol. 20, no. 2, pp. 740–749, 2015.
- [38] C. T. Chen and H. V. Pham, “Trajectory planning in parallel kinematic manipulators using a constrained multi-objective evolutionary algorithm,” *Nonlinear Dynamics*, vol. 67, no. 2, pp. 1669–1681, 2012.
- [39] R. Kelaiaia, O. Company, and A. Zaatri, “Multiobjective optimization of a linear Delta parallel robot,” *Mechanism and Machine Theory*, vol. 50, pp. 159–178, 2012.
- [40] P. K. Jamwal, S. Xie, and K. C. Aw, “Kinematic design optimization of a parallel ankle rehabilitation robot using modified genetic algorithm,” *Robotics and Autonomous Systems*, vol. 57, no. 10, pp. 1018–1027, 2009.
- [41] Z. Gao, D. Zhang, and Y. Ge, “Design optimization of a spatial six degree-of-freedom parallel manipulator based on artificial intelligence approaches,” *Robotics and Computer-Integrated Manufacturing*, vol. 26, no. 2, pp. 180–189, 2010.
- [42] G. Wang, Y. Wang, J. Zhao, and G. Chen, “Process optimization of the serial-parallel hybrid polishing machine tool based on artificial neural network and genetic algorithm,” *Journal of Intelligent Manufacturing*, vol. 23, no. 3, pp. 365–374, 2012.